中国激光

热等静压处理对选区激光熔化GH3536微观结构及拉伸性能的影响

林可欣，刘秀国，龚宝明*，王颖
天津大学材料科学与工程学院，天津 300350

摘要 利用选区激光熔化技术制备GH3536试样，研究了热等静压处理前、后选区激光熔化GH3536微观结构演变对力学性能各向异性的影响。利用扫描电镜、电子背向散射衍射和拉伸试验等方法对沉积态和热等静压态试样进行了微观组织、晶体织构和力学性能表征分析。研究结果表明，与传统工艺相比沉积态试样形成了超细晶组织且拉伸性能较高。*X*-*Y*面中的等轴晶存在〈001〉和〈101〉择优取向；*Y*-*Z*面中外延生长的柱状晶结构的〈001〉晶向近似与增材方向平行。受晶粒尺寸及织构强度的影响，相对于纵向试样，横向试样的屈服和抗拉强度更高，但其延展性偏低，在断口中观察到脆性断裂特征及未熔合缺陷。经热等静压处理后，柱状晶粒发生等轴化转变，晶粒取向随机分布，碳化物沿晶界析出，裂纹愈合，但是试样拉伸强度降低，塑性升高，并且各向异性消失。

关键词 激光技术；选区激光熔化；GH3536合金；热等静压；微观结构；拉伸性能
中图分类号 TG113.1；TG113.2；TG456.7 **文献标志码** A **DOI**：10.3788/CJL220663

1 引 言

GH3536作为一种典型的固溶强化镍基合金，具有良好的抗氧化性、抗热腐蚀性及抗疲劳性，被广泛应用于航空发动机燃烧室部件以及其他一些长期在高温中服役的零部件中[1-3]。但航空发动机燃烧室部件的结构复杂、内部流道多，传统的加工制造工艺已经无法满足制造需求[4-5]。

选区激光熔化(SLM)技术作为目前最流行的增材制造工艺之一，以数字模型为基础，通过高能量密度的激光束熔化金属粉末，通过层层堆叠得到实体零件。与传统的减材制造方法相比，SLM技术在节约材料、工艺控制和零件性能等方面具有很大的优势，特别适用于航空发动机燃烧室零部件的加工[6-8]。

目前，利用SLM技术生产镍基高温合金面临的主要挑战包括由工艺引发的缺陷、微观偏析和由微观结构不均匀导致的力学性能的各向异性。国内外对选区激光熔化GH3536已经进行了一些研究。Montero-Sistiaga等[9]比较了低功率和高功率下构件的微观机构和拉伸性能，发现高激光功率导致熔池形状宽而浅，从而使增材方向的织构强度增大。Wang等[10]研究了激光功率、扫描速率、扫描间距对成形合金显微组织、拉伸性能、尺寸精度等的影响，通过优化工艺参数，获得了质量最佳的零件。Cheng等[11]通过调节热处理制度，优化了Hastelloy X样品的微观结构并改善了其力学性能。Pourbabak等[12]发现热等静压(HIP)处理后晶界上析出$Cr_{23}C_6$，同时晶粒内部硬度明显下降。但这些研究主要集中在工艺参数和热处理制度对SLM成形性能的影响。由于SLM技术的工艺特点，其成形合金在增材方向(building direction)和激光扫描方向(scanning direction)上的组织和性能存在明显差异，不同方向上的性能差异对零件的应用具有重要意义。同时，热等静压处理虽然能大幅减少SLM成形过程中产生的缺陷，但对其力学性能有较大影响。所以有必要对热等静压处理前、后SLM成形合金的组织改变及力学性能各向异性的转变进行研究。但国内关于SLM成形GH3536合金微观结构不均匀引起的力学性能各向异性的研究较少，同时结合热处理的对比研究更是鲜有报道。

本文以SLM成形GH3536试样为研究对象，分别对沉积态和热等静压试样的微观结构和晶体学织构特征进行了表征，并结合力学性能及断口形貌重点讨论了合金力学性能的各向异性及原因，同时分析了热等静压处理对SLM成形GH3536各向异性的影响。研究结果为SLM成形GH3536合金的实际应用提供了一定的参考。

2 试验材料及方法

本试验选用气雾化球形GH3536合金粉末作为

收稿日期：2022-03-14；**修回日期**：2022-04-14；**录用日期**：2022-05-05；**网络首发日期**：2022-05-15
基金项目：国家自然科学基金(51875402)
通信作者：*gong_bm@tju.edu.cn

SLM 沉积原料，粉末粒度为 15～45 μm，其化学成分如表 1 所示。

表 1　GH3536 合金粉末化学成分

Table 1　Chemical compositions of GH3536 alloy powder

Element	Cr	Fe	Mo	Co	W	Si	C	Ni
Mass fraction /%	20.50–23.00	17.00–20.00	8.00–10.00	0.50–2.50	0.20–1.00	≤1.00	≤0.15	Bal.

选区激光熔化 GH3536 试样的主要工艺参数如下：扫描速度为 1100 mm/s，激光功率为 200 W，最小层厚为 20 μm，扫描间距为 90 μm，层间扫描转角为 67°，整个制备过程在氩气保护气氛下进行，试样分别沿水平方向（横向）和垂直方向（纵向）堆叠，如图 1 所示，其中 n 为层编号。SLM 成形结束后采用线切割方法将试样从基板上分离，记为沉积态试样（SLM 试样）；将热等静压处理（处理温度为 1180 ℃，处理压强为 150 MPa，处理时间为 3 h）后的试样记为 HIP 试样。利用线切割机将制备好的试样切割成块状金相试样和室温拉伸试样，具体尺寸如图 2 所示。

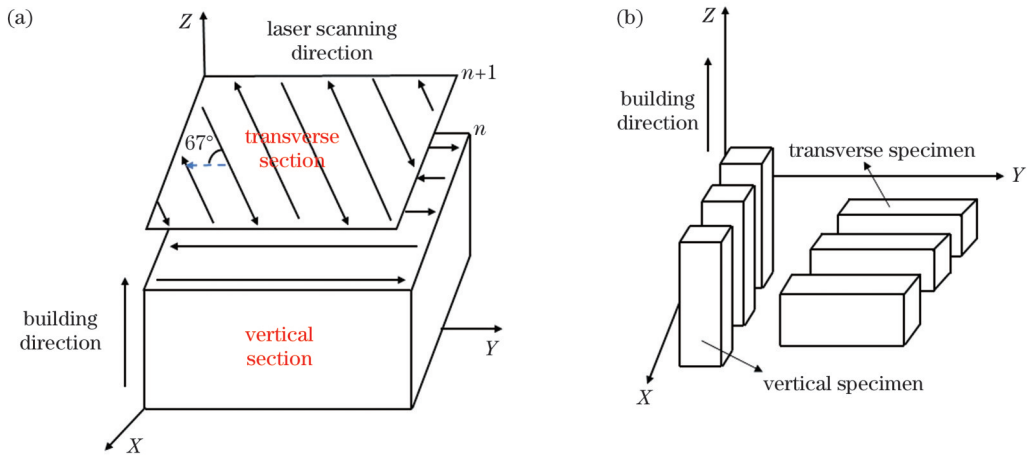

图 1　SLM 试样制备。(a)扫描策略；(b)SLM 试样

Fig. 1　SLM sample preparation. (a) Scanning strategy; (b) SLM specimen

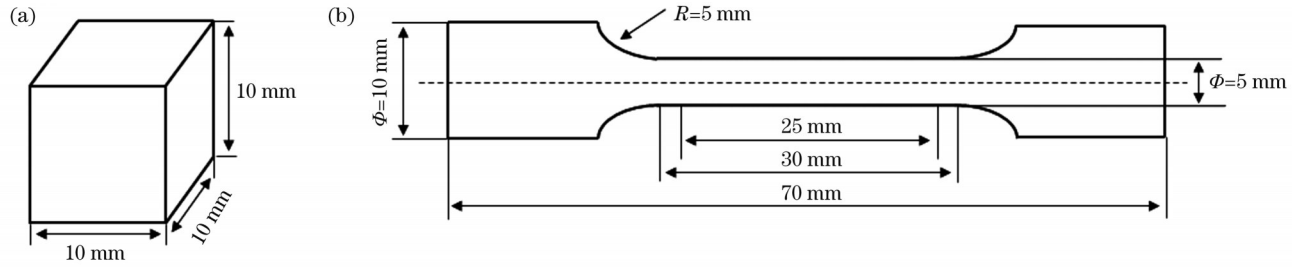

图 2　试样尺寸示意图。(a)金相试样；(b)拉伸试样

Fig. 2　Schematics of sample size. (a) Metallographic sample ; (b) tensile sample

用砂纸打磨块状试样的 X-Y 平面和 Y-Z 平面，随后用金刚石抛光剂抛光。抛光后的试样采用王水试剂（HNO_3 和 HCl 的体积比为 1∶3）进行金相腐蚀，腐蚀时间为 10 s，然后通过光学显微镜（OM）和扫描电镜（SEM）观察试样的微观结构。利用能谱仪（EDS）对析出相进行能谱扫描。使用体积分数为 5% 的高氯酸分别对机械抛光后的样品进行电解抛光，通过电子背向散射衍射（EBSD）测试分析材料的晶体结构。最后在室温下使用万能拉伸试验机以 5 mm/min 的速率对横向和纵向试样进行拉伸测试，并对拉伸断口进行观察。

3　结果与讨论

3.1　显微组织

SLM 试样 X-Y 平面和 Y-Z 平面的微观组织如图 3 所示，可以发现，沉积态试样中的熔池形态清晰可见，层间扫描转角为 67°，在激光束照射下纵截面中的粉末熔化，形成了近似半球形的熔池，熔池宽度为 60～90 μm。相邻扫描轨道及相邻扫描层之间的搭接良好，几乎没有层间间隙。熔池内部存在裂纹缺陷，且 Y-Z 面中的裂纹倾向于与增材方向平行，X-Y 面中的裂纹方向随机分布。

SLM 具有极快的冷却速度，形成的超细晶组织不

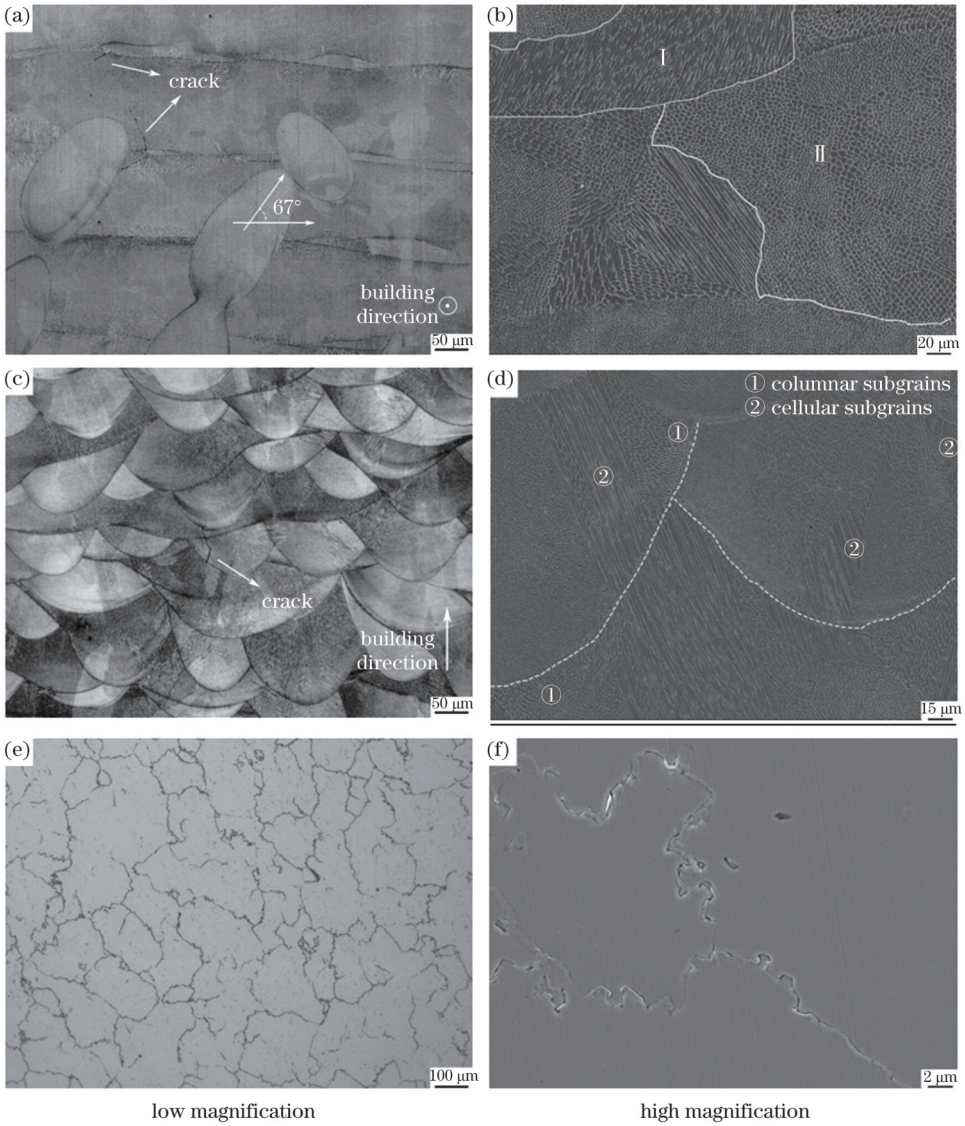

图 3　试样显微组织图。(a)(b)沉积态试样 *X*-*Y* 面;(c)(d)沉积态试样 *Y*-*Z* 面;(e)(f)HIP 试样

Fig. 3　Microstructures of sample. (a)(b) *X*-*Y* plane of SLM sample; (c)(d) *Y*-*Z* plane of SLM sample; (e)(f) HIP sample

同于传统工艺。在高倍镜下发现 SLM 试样组织由柱状晶和胞晶组成,*X*-*Y* 面中晶粒大多为细小的胞状亚晶,胞状亚晶的尺寸约为 1 μm,亚晶生长方向存在差异,如图 3(b)中Ⅰ区和Ⅱ区所示,造成这一现象的原因是粗晶生长取向的差异。在 *Y*-*Z* 面中大量柱状晶垂直于熔合线沿增材方向外延生长,如图 3(c)、(d)所示,这是由于液态金属在结晶时以下层已凝固熔池为基底进行非均质形核,而熔池的散热方向与温度梯度方向相反,因此晶核垂直于熔池的固液界面并沿温度梯度反方向生长,从而 SLM 成形的柱状晶呈典型的外延生长的特点。与此同时,液态金属与周围环境之间的温度梯度引起了 Benard 对流和 Marangoni 对流,使柱状晶在不同区域的取向存在细微差异[13-15]。此外,在选区激光熔化过程中,由于熔体沿竖直方向运动且温度梯度大,因此熔池边缘多为六角胞状结构,而熔池中心到边缘区域的熔体处于水平流动状态,形成了较长的对流区域,最终部分熔体凝固为柱状亚晶结构,如图 3(d)所示。

图 3(e)、(f)为 HIP 试样的 *X*-*Y* 面显微组织。可以看到,热等静压处理后试样表面原有的熔池形貌和激光扫描痕迹完全消失,试样中很难观察到胞状和柱状亚晶。试样发生了晶粒再结晶,消除了组织的各向异性,故此处仅展示 *X*-*Y* 面的显微组织。热处理后的晶界呈弯曲的锯齿状,大量析出相出现在晶界附近。同时,经过热等静压处理后试样中的裂纹在高温高压下得到了焊合。

为了确定 HIP 试样中晶界析出物的元素组成,通过 EDS 对其进行了线扫描和点分析,如图 4 所示。从线扫描得到的元素分布可以看到,明显的富 Cr 的微观偏析现象以及少量 Mo 元素的富集现象出现在晶界附近。点分析结果如图 4(c)、(d)所示,析出相中 Cr 的含量(质量分数)为 50.94%,而基体中 Cr 的含量(质量分数)仅为 21.18%。此外,发现析出相中钼含量(质量分数为 16.73%)约为基体中钼含量(质量分数为

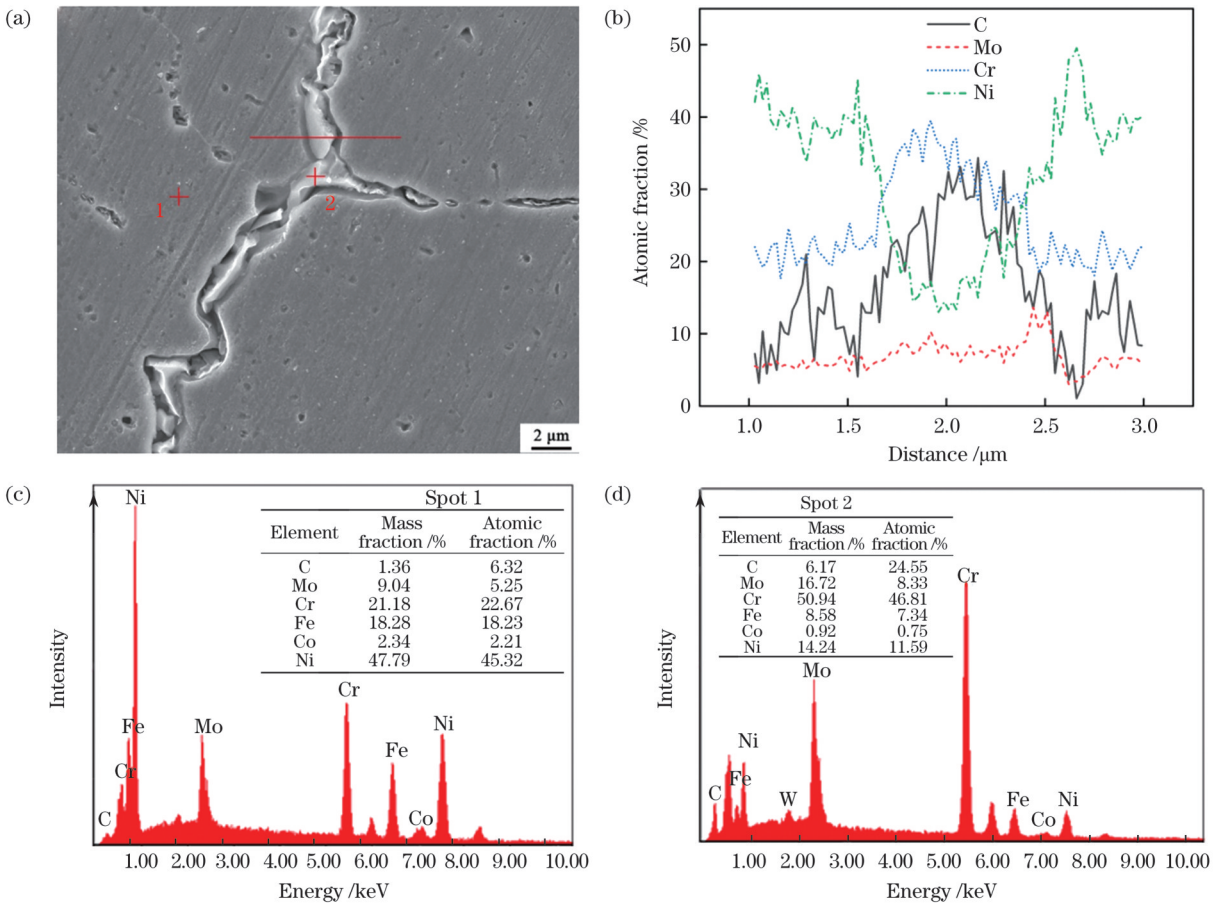

图 4　析出相的 EDS 分析结果。(a)析出相的 SEM 图;(b)线扫结果;(c)(d)点分析结果

Fig. 4　EDS analysis results of precipitated phase. (a) SEM image of precipitated phase; (b) line scan result; (c)(d) spot analysis results

9.04%)的 2 倍。EDS 分析结果表明,析出相主要为富铬的 $M_{23}C_6$ 碳化物和富钼的 M_6C 碳化物,这与 Montero-Sistiaga 等[16]的研究结果相符。

3.2　晶粒大小及取向

EBSD 结果(图 5)表明,SLM 试样的 *X*-*Y* 面和 *Y*-*Z* 面在晶粒尺寸和晶体取向方面存在显著差异:*X*-*Y* 面中的晶粒为近似等轴晶,晶粒平均直径为 22.9 μm,且晶粒沿〈001〉和〈101〉方向存在轻微择优取向;而 *Y*-*Z* 面中的晶粒则呈是沿增材方向生长的柱状晶,平均晶粒长宽比为 2.64,平均晶粒直径为 29.56 μm,晶粒方向整体表现为随机取向。此外,根据极图(PF)结果[图 5(d)、(e)]发现,在 SLM 试样的 *X*-*Y* 及 *Y*-*Z* 面内均存在强{100}织构分量,且 *Y*-*Z* 面中〈001〉晶向近似与增材方向平行。这是因为在增材制造过程中熔池向基板的传热方向与增材方向平行,而立方晶系沿〈001〉方向生长最快,所以可以观察到具有立方结构的柱状晶的〈001〉晶向近似与增材方向平行。

从图 5(c)、(f)可以看到,经热处理后晶粒的择优取向特性消失,晶粒取向随机分布。沿横/纵截面均为等轴晶粒,晶粒平均直径为 23.9 μm。这是由于相比于沉积态,热等静压处理抑制了再结晶过程中的晶粒长大,晶粒没有明显粗化,同时再结晶使{100}、{110}和{111}面出现强度相近的随机织构。

此外,根据取向角的大小,晶界可分为小角度(2°<θ<15°)晶界(LAGBs)和大角度(θ>15°)晶界(HAGBs)。根据晶界图(图 6)可知,在沉积态试样的晶粒内部分布着大量小角度晶界,SLM 试样 *X*-*Y* 及 *Y*-*Z* 面中的小角度晶界数量占比分别为 67% 和 73%,热处理后其比例均降为 24%。图 6(d)进一步显示了不同状态下的晶粒错向角分布情况。可以看到,经过热等静压处理后小角度晶界减少,在晶界错向角分布图中,60°处出现峰值。60°的大角度晶界主要是孪晶界,这说明再结晶过程中形成的大量孪晶界与 LAGBs 的演变有关。

3.3　拉伸性能

图 7 为沉积态和热等静压态试样的具体拉伸性能。如图 7(b)所示,沉积态的横向试样和纵向试样在强度和韧性方面存在明显的各向异性:横向试样的屈服强度为 761 MPa,抗拉强度为 850 MPa,均高于纵向试样;横向试样的断后伸长率为 28%,断面收缩率为 33%,均低于纵向试样。Tomus 等[17]也有类似发现。究其原因,可能与两个方向上的晶粒尺寸和晶体织构的差异有关。如上所述,试样中 *X*-*Y* 面和 *Y*-*Z* 面内存在不同强度的织构(图 5),而晶体结构对材料塑性变形能力的影响可以通过 Schimd 定律来表征[18]:

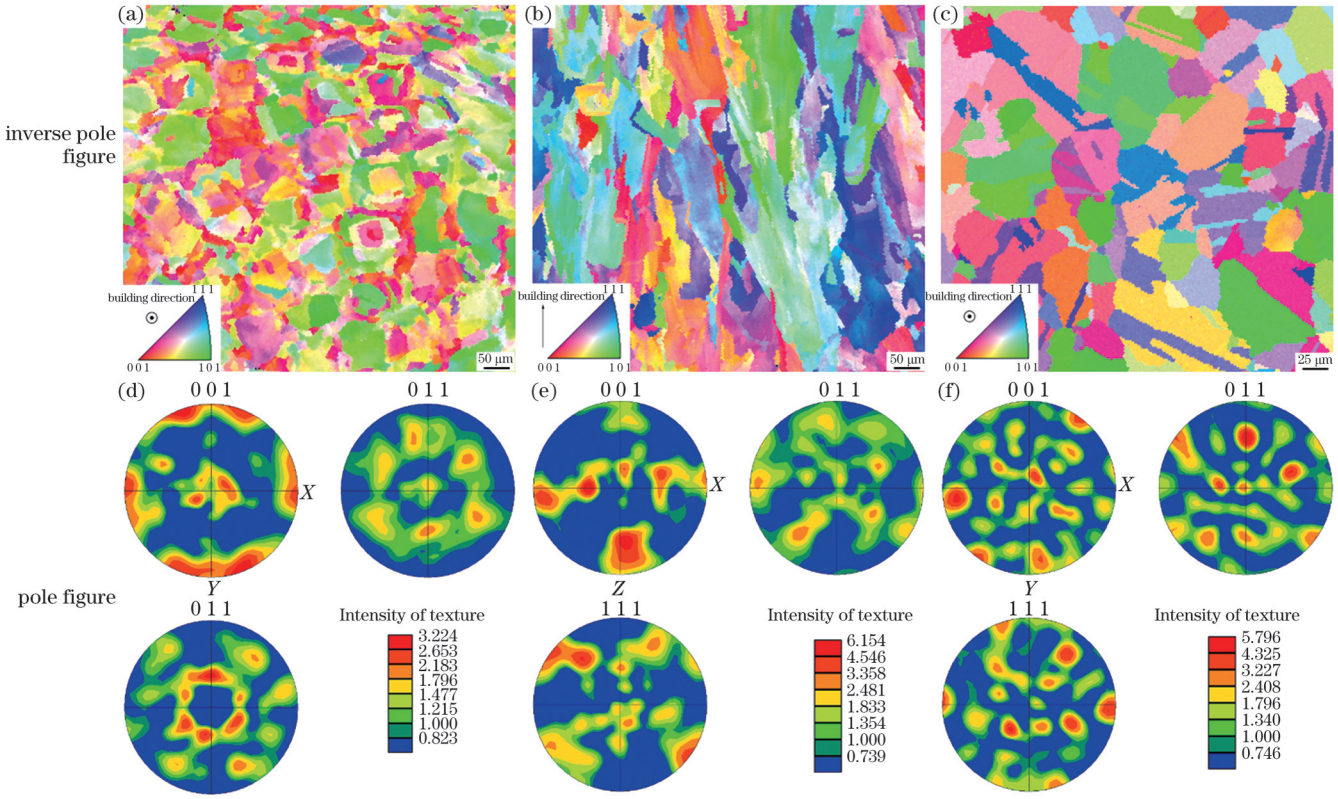

图 5　EBSD 反极图和极图。(a)(d)沉积态试样 *X*-*Y* 面；(b)(e)沉积态试样 *Y*-*Z* 面；(c)(f)HIP 试样

Fig. 5　EBSD inverse pole figures and pole figures. (a)(d) *X*-*Y* plane of SLM sample; (b)(e) *Y*-*Z* plane of SLM sample; (c)(f) HIP sample

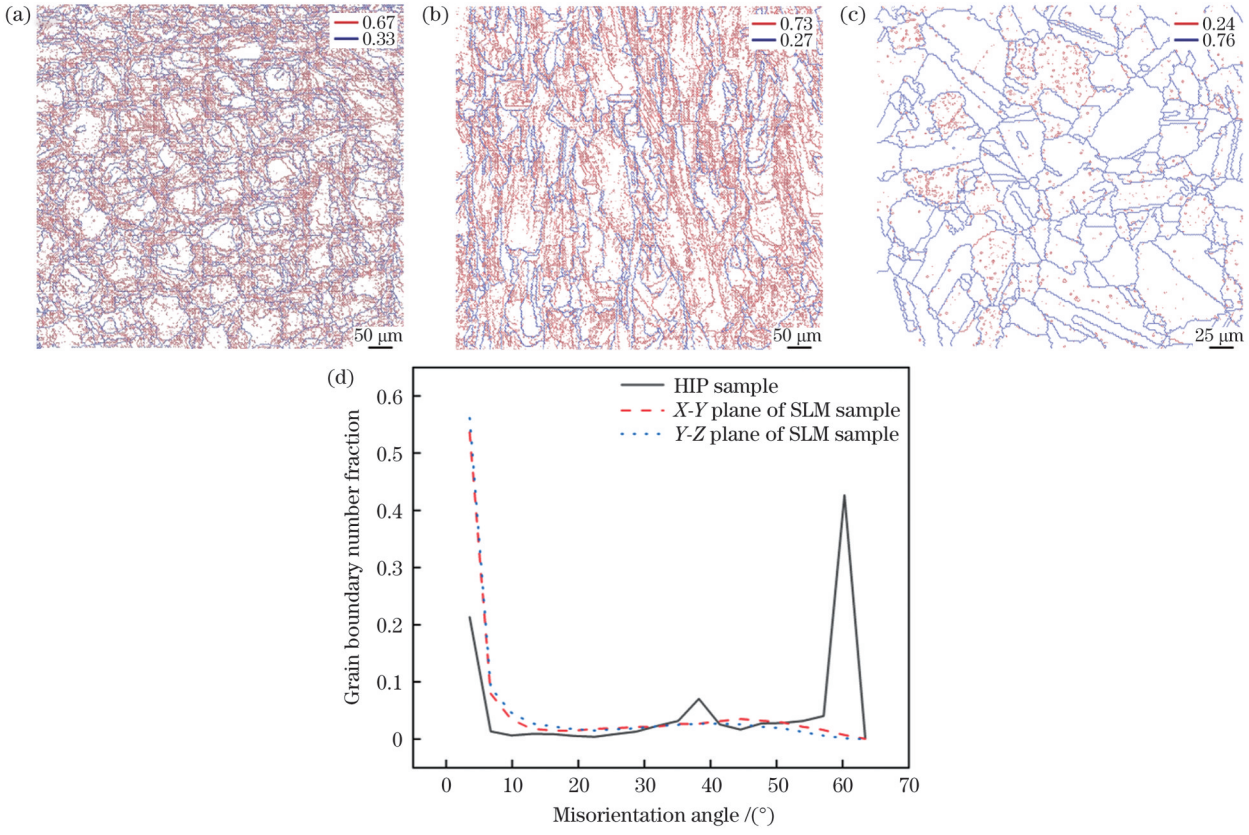

图 6　晶界特征。(a)沉积态试样 *X*-*Y* 面；(b)沉积态试样 *Y*-*Z* 面；(c)HIP 试样；(d)晶界错向角分布

Fig. 6　Grain boundary characteristics. (a) *X*-*Y* plane of SLM sample; (b) *Y*-*Z* plane of SLM sample; (c) HIP sample; (d) grain boundary misorientation angle distribution

$$\tau_c = \sigma_s \cos\lambda \cos\varphi \ , \tag{1}$$

式中：$\cos\lambda\cos\varphi$ 为施密特因子；$\lambda=\pi/2-\varphi$；φ 为滑移面法线与外力夹角；τ_c 为材料固有系数，由材料本身决定；σ_s 为材料的屈服强度。只有当滑移面滑移方向上的剪应力达到临界值时，材料才会通过初始滑移系统发生塑性变形，因此施密特因子越高，滑移越容易发生，材料的屈服强度就越低。计算可知，*X*-*Y* 面和 *Y*-*Z* 面的施密特因子分别为 0.4749 和 0.4894，这意味着 SLM 横向试样能表现出更高的屈服强度。此外，由 Hall-Petch 关系[19]可知，屈服强度 σ_s 与晶粒尺寸相关：

$$\sigma_s = \sigma_0 + \frac{K}{\sqrt{d_{\text{mean}}}}, \tag{2}$$

式中：σ_0 和 K 为材料常数；d_{mean} 为晶粒平均尺寸。根据位错理论，晶界在位错滑移过程中起到阻碍作用，而晶粒越细晶界就越多，对位错运动的阻碍作用也更大，进而使得静态强度越高。综上所述，试样沿扫描方向的晶粒尺寸小于沿增材方向的晶粒尺寸，所以横向试样具有更高的屈服强度。

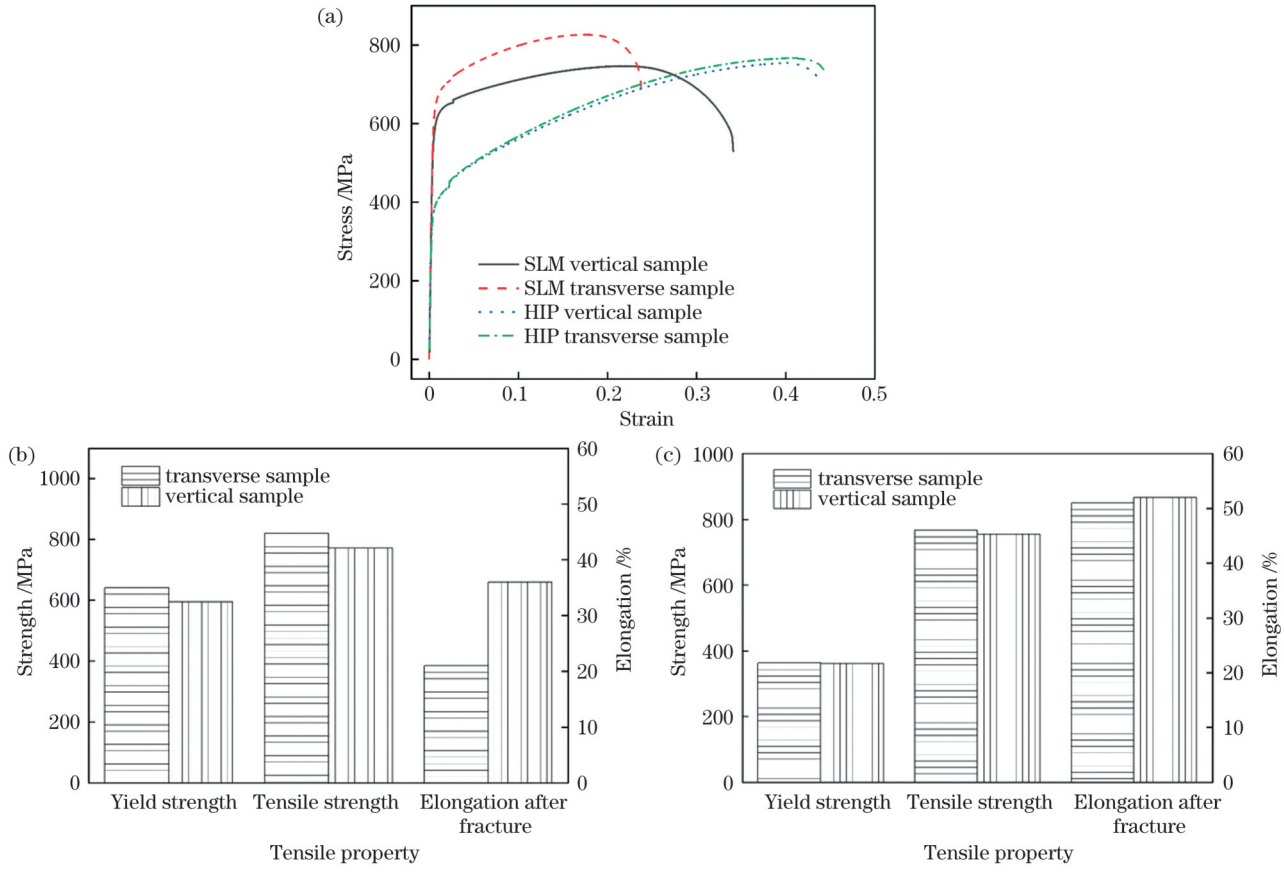

图 7　拉伸性能。(a)应力-应变曲线；(b)SLM 试样的拉伸性能；(c)HIP 试样的拉伸性能

Fig. 7　Tensile properties. (a) Stress-strain curve; (b) tensile properties of SLM sample; (c) tensile properties of HIP sample

经热处理后试样的拉伸性能在水平和垂直方向上基本表现为各向同性，如图 7(c)所示。对比发现，HIP 试样的屈服强度明显低于沉积态试样，而断后延伸率却升高。这主要归因于试样内部晶界形态的变化和缺陷的消除。一方面，根据文献[20]可知，SLM 试样中的亚晶在变形过程中可视为 LAGBs，起到晶界强化作用。热处理后晶内亚晶结构消失，导致晶界强化作用减弱，使试样的屈服强度有所下降。另一方面，热等静压处理后裂纹发生闭合，孔隙缺陷数量减少，致密度提高，同时热处理消除了部分残余应力，最终使 HIP 试样的屈服强度下降，韧性提高。

3.4　断口形貌

为了进一步研究断裂机制，分别对沉积态和 HIP 态试样的断口形貌进行观察。沉积态纵向试样和横向试样的断口形貌分别如图 8 和图 9 所示，在试样断口处均观察到随机分布的微孔。横向试样断口有准解理面、解理台的形貌，且韧窝尺寸明显大于纵向试样，试样总体表现为韧性-脆性混合断裂模式。此外，在断口边缘还观察到一些孔隙缺陷以及未熔化的粉末颗粒[图 8(c)]，这些缺陷在应力作用下很可能发展成为裂纹萌生源，破坏试样的微观结构稳定性，从而降低延展性。相比之下，纵向试样的断口表面凹凸不平，存在大量 1～2 μm 尺寸的微小韧窝，说明该处在断裂前经历了较强的塑性变形过程，是典型的韧性断裂。除此之外，纵向试样的断口形貌存在于 *X*-*Y* 面内，试样内部存在方向不一的微裂纹，在拉应力的作用下，残余热应力所产生的一次裂纹扩展产生二次裂纹，裂纹的数量

和长度都呈增加的趋势，因此在试样的断口形貌中可观察到较多的裂纹。横向试样的断口形貌存在于 *Y*-*Z* 面内，*Y*-*Z* 面内的裂纹走向大致相同，失效模式为穿晶断裂，在拉应力作用下，一次裂纹快速扩展，没有异向裂纹开裂相互阻碍的情况出现，因此横向试样的韧性较差。

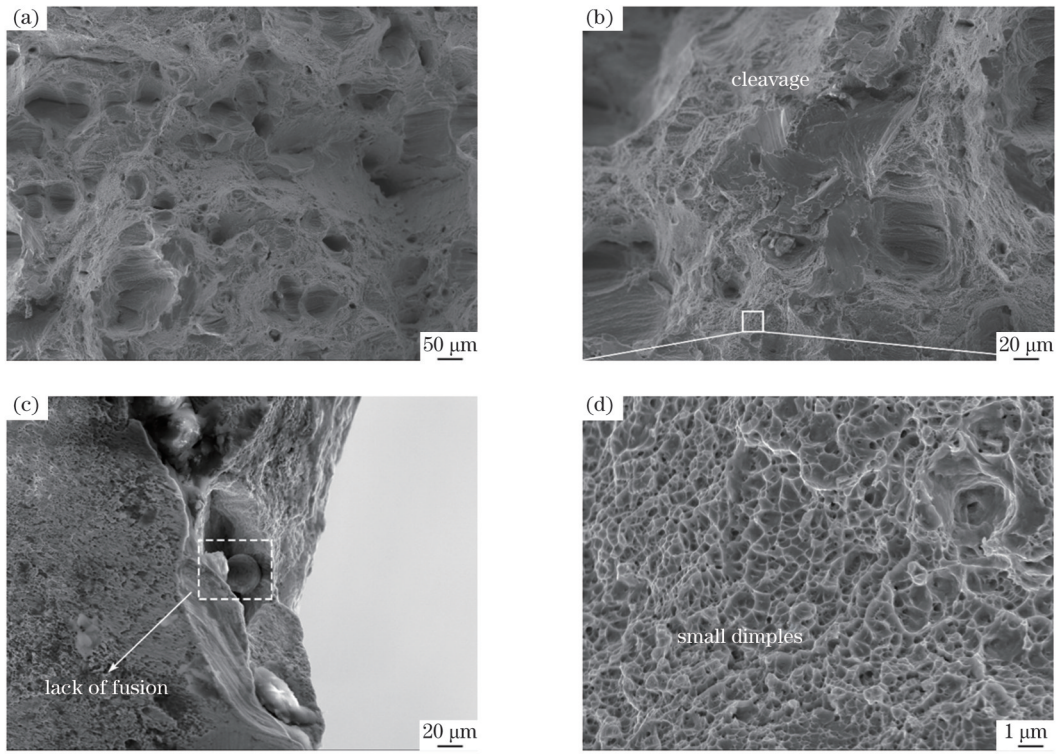

图 8　SLM 横向试样的断口特征。(a)断口形貌；(b)解理面；(c)未熔合缺陷；(d)韧窝

Fig. 8　Fracture characteristics of SLM transverse sample. (a) Fracture morphology; (b) cleavage plane; (c) lack of fusion defect; (d) dimples

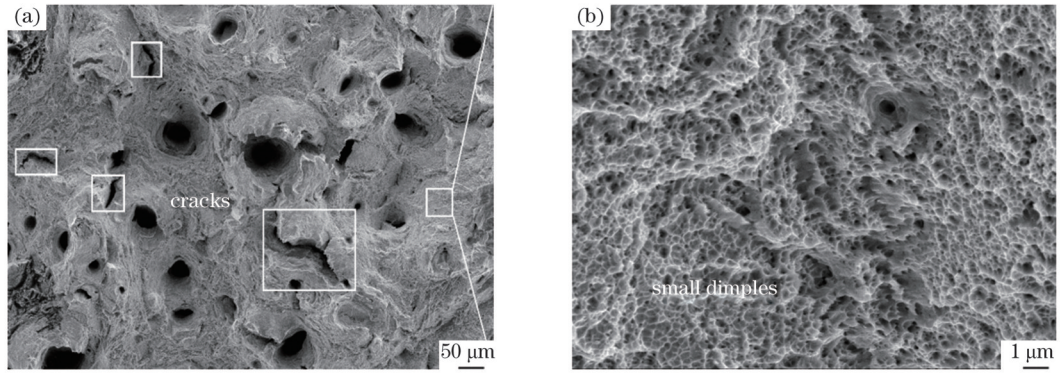

图 9　SLM 纵向试样的断口特征。(a)断口形貌；(b)韧窝

Fig. 9　Fracture characteristics of SLM vertical sample. (a) Fracture morphology; (b) dimples

HIP 试样的断口形貌如图 10 所示，发现横向试样和纵向试样的断口没有显著差异，失效模式均为韧性断裂。但相比于沉积态，断口表面的孔隙和微裂纹数量大大减少，不存在未熔合缺陷。同时韧窝更深，这也是其延伸率明显高于沉积态的主要原因。

4　结　　论

通过对不同状态下选区激光熔化成形 GH3536 镍基高温合金的微观结构和力学性能进行研究，得到如下结论：

1）在选区激光熔化过程中，因其极高的温度梯度和冷却速率，形成了胞状和柱状亚晶。在 Benard 对流和 Marangoni 对流作用下，胞状亚晶多在熔池边界处产生，柱状亚晶多分布于熔池内部，同时试样内部存在裂纹和孔隙等缺陷。热等静压处理后，亚晶结构消失，裂纹发生闭合，晶界处存在 C、Cr 和 Mo 的偏析。

2）沉积态试样的晶体生长方向受最大温度梯度和晶体学择优取向的竞争影响。沿扫描方向，等轴晶存在〈001〉和〈101〉择优取向。由于温度梯度方向与增材方向趋于一致，在增材方向上存在垂直熔池外延生长

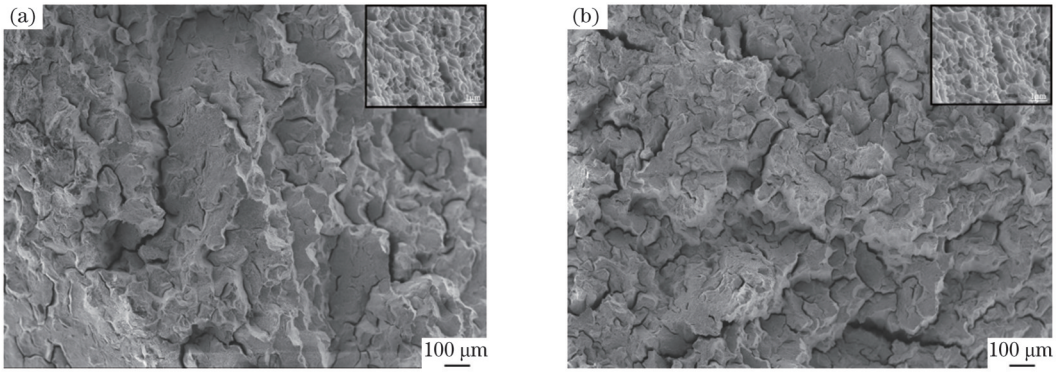

图 10 HIP试样的断口形貌。(a)横向试样;(b)纵向试样

Fig. 10 Fracture morphologies of HIP sample. (a) Transverse sample; (b) vertical sample

的柱状晶,且〈001〉晶向与增材方向平行。热等静压处理后,再结晶使晶粒无明显择优取向,晶粒表现为细小的等轴晶。

3)受晶粒尺寸、晶体织构和微观缺陷的影响,沉积态试样的力学性能存在显著的各向异性,热等静压处理消除了微观组织的各向异性,拉伸性能表现为各向同性。与沉积态相比,HIP试样中的小角度晶界明显减少,出现孪晶,同时试样致密度增大,其屈服强度下降约39%,但延伸率升高了约42%。

4)沉积态横向试样的断口特征为韧性-脆性混合断裂,而纵向试样的断口特征为典型的韧性断裂。相比于沉积态,虽然HIP试样仍为韧性断裂,但是断口表面的韧窝更深,孔隙和微裂纹数量大大减少,未熔合缺陷消失。

参 考 文 献

[1] Zhang D X, Wang J P, Wen Z X, et al. V-notched bar creep life prediction: GH3536 Ni-based superalloy under multiaxial stress state[J]. Journal of Materials Engineering and Performance, 2016, 25(7): 2959-2968.

[2] 刘浩, 王心美, 刘大顺, 等. 缺口对GH3536镍基高温合金蠕变性能的影响[J]. 稀有金属材料与工程, 2014, 43(10): 2473-2478.
Liu H, Wang X M, Liu D S, et al. Influence of Notch on creep properties of GH3536 nickel-based superalloy[J]. Rare Metal Materials and Engineering, 2014, 43(10): 2473-2478.

[3] 《中国航空材料手册》编辑委员会. 中国航空材料手册[M]. 北京: 中国标准出版社, 2002.
Editing Board of China Aeronautical Materials Handbook. China Aeronautical Materials Handbook[M]. Beijing: Standards Press of China, 2002.

[4] Herzog D, Seyda V, Wycisk E, et al. Additive manufacturing of metals[J]. Acta Materialia, 2016, 117: 371-392.

[5] Yadollahi A, Shamsaei N. Additive manufacturing of fatigue resistant materials: challenges and opportunities[J]. International Journal of Fatigue, 2017, 98: 14-31.

[6] 赵志国, 柏林, 李黎, 等. 激光选区熔化成形技术的发展现状及研究进展[J]. 航空制造技术, 2014, 57(19): 46-49.
Zhao Z G, Bai L, Li L, et al. Status and progress of selective laser melting forming technology[J]. Aeronautical Manufacturing Technology, 2014, 57(19): 46-49.

[7] 闫雪, 阮雪茜. 增材制造技术在航空发动机中的应用及发展[J]. 航空制造技术, 2016, 59(21): 70-75.
Yan X, Ruan X Q. Application and development of additive manufacturing technology in aeroengine[J]. Aeronautical Manufacturing Technology, 2016, 59(21): 70-75.

[8] Yadroitsev I, Bertrand P, Smurov I. Parametric analysis of the selective laser melting process[J]. Applied Surface Science, 2007, 253(19): 8064-8069.

[9] Montero-Sistiaga M L, Pourbabak S, van Humbeeck J, et al. Microstructure and mechanical properties of Hastelloy X produced by HP-SLM (high power selective laser melting)[J]. Materials & Design, 2019, 165: 107598.

[10] Wang F, Wu X H, Clark D. On direct laser deposited Hastelloy X: dimension, surface finish, microstructure and mechanical properties[J]. Materials Science and Technology, 2011, 27(1): 344-356.

[11] Cheng X P, Du Z F, Chu S X, et al. The effect of subsequent heating treatment on the microstructure and mechanical properties of additive manufactured Hastelloy X alloy[J]. Materials Characterization, 2022, 186: 111799.

[12] Pourbabak S, Montero-Sistiaga M L, Schryvers D, et al. Microscopic investigation of as built and hot isostatic pressed Hastelloy X processed by selective laser melting[J]. Materials Characterization, 2019, 153: 366-371.

[13] Chakraborty N. The effects of turbulence on molten pool transport during melting and solidification processes in continuous conduction mode laser welding of copper-nickel dissimilar couple[J]. Applied Thermal Engineering, 2009, 29(17/18): 3618-3631.

[14] 周洋. 具有水平流动的Rayleigh-Benard对流[D]. 西安: 西安理工大学, 2009.
Zhou Y. Rayleigh-Benard convection with lateral flows[D]. Xi'an: Xi'an University of Technology, 2009.

[15] 刘春元. 热毛细对流的研究及其数值模拟[D]. 天津: 河北工业大学, 2003.
Liu C Y. The study and numerical simulation of Marangoni convection[D]. Tianjin: Hebei University of Technology, 2003.

[16] Montero-Sistiaga M L, Liu Z Z, Bautmans L, et al. Effect of temperature on the microstructure and tensile properties of micro-crack free hastelloy X produced by selective laser melting[J]. Additive Manufacturing, 2020, 31: 100995.

[17] Tomus D, Tian Y, Rometsch P A, et al. Influence of post heat treatments on anisotropy of mechanical behaviour and microstructure of Hastelloy-X parts produced by selective laser melting[J]. Materials Science and Engineering: A, 2016, 667: 42-53.

[18] Hosford W F. Mechanical behavior of materials[M]. Cambridge: Cambridge University Press, 2010.

[19] Hansen N. Hall-Petch relation and boundary strengthening[J]. Scripta Materialia, 2004, 51(8): 801-806.

[20] Voisin T, Forien J B, Perron A, et al. New insights on cellular structures strengthening mechanisms and thermal stability of an austenitic stainless steel fabricated by laser powder-bed-fusion[J]. Acta Materialia, 2021, 203: 116476.

Effects of Hot Isostatic Pressing on Microstructure and Tensile Properties of GH3536 Manufactured Using Selective Laser Melting

Lin Kexin, Liu Xiuguo, Gong Baoming*, Wang Ying

School of Materials Science and Engineering, Tianjin University, Tianjin 300350, *China*

Abstract

Objective The production of nickel-based high-temperature alloys using selective laser melting (SLM) technology offers significant advantages in terms of material savings, process control, and product performance. However, the use of SLM technology presents several challenges, such as process-induced defects, microsegregation, and anisotropy of the mechanical properties owing to microstructural inhomogeneities. Although several studies on SLM GH3536 have been conducted worldwide, these studies have primarily focused on the effects of process parameters and heat treatment processes on the formability of SLM. Owing to the process characteristics of SLM technology, substantial differences exist in the microstructure and properties of the alloys formed in the additive and laser scanning directions, and these differences have a significant impact on their application. Simultaneously, hot isostatic pressing (HIP) treatment can significantly reduce the defects formed during the SLM process and has a significant impact on the mechanical properties of the material. Therefore, it is necessary to examine the changes in the microstructure and anisotropy of the mechanical properties of SLM-formed alloys before and after HIP. However, there are few systematic studies on the anisotropy of the mechanical properties of SLM-formed GH3536 alloys due to microstructural inhomogeneities, and comparative studies in conjunction with heat treatment are rarely reported in the scientific literature. Using SLM-formed GH3536 specimens as the research object, the microstructure and crystallographic texture characteristics of deposited and HIP specimens are characterized in this study. Additionally, the anisotropy of the mechanical properties of the alloy and its causes are discussed on the basis of the mechanical properties and fracture morphology. Moreover, the effect of HIP on the anisotropic behavior of SLM-formed GH3536 is investigated. This study provides a reference for the practical application of SLM-formed GH3536 alloys.

Methods SLM GH3536 specimens were prepared using SLM equipment, and HIP was applied to the SLM-formed specimens. Using a wire-cutting machine, the prepared samples were then cut into bulk metallographic samples and room-temperature tensile samples. The *X*-*Y* and *Y*-*Z* planes of the block specimens were polished using sandpaper, followed by diamond polishing. The as-polished samples were etched for 10 s using aqua regia, and their microstructures were observed via optical microscopy (OM) and scanning electron microscopy (SEM). The mechanically polished samples were electropolished with perchloric acid, and the electron backscatter diffraction (EBSD) technique was used to analyze the crystal structures of the materials. Finally, the transverse and vertical tensile specimens were tested at a rate of 5 mm/min using a universal tensile testing machine at room temperature, and the corresponding tensile fractures were observed.

Results and Discussions As depicted in Figs. 3 and 5, the microstructure of SLM GH3536 exhibits clear anisotropy. The grains in *X*-*Y* plane comprise equiaxed crystals with 〈001〉 and 〈101〉 preferred orientations, whereas the grains in *Y*-*Z* plane are epitaxial columnar crystals. Additionally, the 〈001〉 crystal direction is roughly parallel to the direction of material addition. Moreover, the SLM specimen exhibits strong {100} texture components in both the *X*-*Y* and *Y*-*Z* planes. As a result of the extremely rapid cooling rate of SLM, columnar and cellular subgrains are formed that are distinct from those produced via conventional processes. Cracks are also observed in the molten pool; those in the *Y*-*Z* plane tend to be parallel to the additive direction, while those in the *X*-*Y* plane are randomly distributed. After the HIP treatment, the original melt pool morphology and laser scanning traces on the surface of the specimen completely disappear, and it is difficult to observe the subgrain structure in the specimen (Figs. 3 and 5). Moreover, a large number of precipitated phases exists along the grain boundaries, and EDS results reveal that the precipitated phases are chromium-rich $M_{23}C_6$ carbides and molybdenum-rich M_6C carbides (Fig. 4). Cracks in the heat-treated specimens are welded simultaneously. A large number of twin boundaries are formed during recrystallization and are related to the evolution of the low-angle boundaries (LAGBs), as indicated by the grain boundary characteristic diagram (Fig. 6). The tensile properties of the SLM specimens are anisotropic (Fig. 7), with the transverse specimens exhibiting higher strength but less toughness. After heat treatment, the tensile properties of the heat-treated specimens are essentially isotropic; the yield strength of the HIP specimens is decreased, and the toughness is increased as a result of the decrease in LAGBs and the increase in densities. In addition, the fracture morphology (Figs. 8 and 9) reveals that the SLM specimens exhibit the mixed tough-brittle

fracture in the transverse direction and the typical ductile fracture in the vertical direction, whereas the HIP specimens exhibit the typical ductile fracture (Fig. 10).

Conclusions The microstructure and mechanical properties of GH3536 nickel-based superalloy formed via SLM during deposition and subsequent heat treatment are investigated in this study, and the following conclusions are drawn. The deposited specimens exhibit ultrafine grain structures and good tensile properties. The preferred orientations of the equiaxed crystals in the X-Y plane are 〈001〉 and 〈101〉, and the 〈001〉 direction of columnar crystal structure grown epitaxially in the Y-Z plane is roughly parallel to the additive direction. Considering the influence of grain size and texture strength, the yield and tensile strengths of the transverse specimen are higher than those of the longitudinal specimen, but their ductility is lower. In addition, brittle fracture characteristics and incomplete fusion defects are observed on the fracture surfaces. Following HIP treatment, the columnar grains undergo an equiaxed transformation; the grain orientation is randomly distributed; carbide precipitation is observed along the grain boundary, and the crack heals. Moreover, the tensile strength of the sample decreases; its plasticity increases, and its anisotropy disappears.

Key words laser technique; selective laser melting; GH3536 alloy; hot isostatic pressing; microstructure; tensile property